Origin of giant dielectric permittivity and localized polarons supported electrical conduction in CaCu3Ti4O12 for extreme environment energy storage applications

Subrata Karmakar

subrata.karmakar@jaipur.manipal.edu

Manipal University Jaipur

K. Ashok

Marri Laxman Reddy Institute of Technology and Management

N. Hussain Basha

CVR College of Engineering

P. K. Koochana

Vardhaman College of Engineering

Rajkumar Boddhula

Vardhaman College of Engineering

M. Patwari

Chaitanya Bharathi Institute of Technology

G. Rajashekhar

Vardhaman College of Engineering

Biman Kar

National Institute of Technology Rourkela

Hari Sankar Mohanty

GIET University

Hitesh Borkar

NIT Warangal

Article

Keywords: Complex double perovskite, Impedance spectroscopy, Giant dielectric constant, AC conductivity, polarons hopping mechanism

Posted Date: November 11th, 2025

DOI: https://doi.org/10.21203/rs.3.rs-8017034/v1

Additional Declarations: No competing interests reported.

Version of Record: A version of this preprint was published at Scientific Reports on February 2nd, 2026.
See the published version at https://doi.org/10.1038/s41598-026-36234-6.

Origin of giant dielectric permittivity and localized polarons supported electrical conduction in $CaCu_3Ti_4O_{12}$ for extreme environment energy storage applications

Subrata Karmakar,[a] K. Ashok,[b] N. Hussain Basha,[c] P. K. Koochana,[d] Rajkumar Boddhula,[d] M. Patwari,[e] G. Rajashekhar,[d] Biman Kar,[f] Hari Sankar Mohanty,[g] Hitesh Borkar,[h]

[a]*Department of Physics, Manipal University Jaipur, Jaipur, Rajasthan 303007, India*
[b]*Department of Physics, Marri Laxman Reddy Institute of Technology and Management, Dundigal, Hyderabad 500043, India.*
[c]*Department of Humanities and Sciences, CVR College of Engineering, Hyderabad, 501510, Telangana, India*
[d]*Department of Chemistry, Vardhaman College of Engineering, Kacharam, Hyderabad, Telangana-501218*
[e]*Department of Chemistry, Chaitanya Bharathi Institute of Technology, Gandipet, Hyderabad, Telangana 500075*
[f]*Department of Physics and Astronomy, National Institute of Technology, Rourkela, Odisha-769008, India*
[g]*Department of Basic Science and Humanities, GIET University, Gunupur, Odisha, 765022, India*
[h]*Department of Physics, NIT Warangal, Telangana-506004, India*
Corresponding email: subrata.karmakar@jaipur.manipal.edu; skarmakarph@gmail.com;

Abstract

We have synthesized $CaCu_3Ti_4O_{12}$ using a green synthesis route, employing an oxalate precursor obtained from a mixture of Averrhoa carambola (star fruit) fruit juice and aloe vera extract. The structural, microstructural, and ac electrical transport characteristics of this material were examined at high temperatures from 308 K to 773 K and in a wide frequency window of 100 Hz to 1 MHz. The Rietveld refinement of X-ray diffraction (XRD) and Raman spectroscopy demonstrates the single-phase body-centered cubic crystal structure with space group *Im-3* and A_g and F_g vibrational modes due to rotations of TiO_6 octahedral and Ti-O-Ti anti-stretching vibrations of $CaCu_3Ti_4O_{12}$. The fitted Nyquist plots (Z' vs. Z'') at different temperatures exhibit the grain and grain boundary contributions, and the semicircles shrink at higher temperatures, which disclosed the negative temperature coefficient of resistance (NTCR) behavior. Both grain (R_g) and grain boundary resistance (R_{gb}) and capacitances (C_g, C_{gb}) diminished with temperature, and their activation energy was estimated to be ~0.56 eV and ~0.84 eV, respectively. The ac electrical conductivity increases with frequency and temperature due to thermally activated charge carriers, and the frequency exponent (n) remains nearly constant at low temperature region (quantum mechanical tunneling model) and decreases after 573 K (correlated barrier hopping model). Their dc activation energy was determined to be 0.51 eV and 0.62 eV, respectively. High dielectric

permittivity (ε_r') ~9458 and low dielectric loss (δ)~0.308 were observed at 308 K and frequency 100 Hz, and both values increase with the evolution of temperatures and quantify a higher ability to store the electrical charges in an electric field. The dielectric relaxations at various temperatures are associated with the Maxwell-Wagner (MW) type polarization, and the distribution of relaxation behavior or Cole-Cole parameter (α) divulged a non-ideal Debye type broader and symmetric distribution with temperatures. The modulus spectra help us to comprehend the origin of the giant dielectric constant and strong interfacial polarization by highlighting the grain and grain boundary contributions. The high dielectric constant, low loss, and high temperature stability recommend its promising applications in several electronic, energy, and sensing applications.

Keywords: *Complex double perovskite; Impedance spectroscopy; Giant dielectric constant; AC conductivity; polarons hopping mechanism;*

1. Introduction:

Recently, high-permittivity (high-k) dielectric materials have garnered a lot of interest because of their critical role in the development of contemporary electronic devices, such as energy storage systems, memory components, capacitors, and sensors. Besides, high-performance dielectric materials are highly desired for miniaturizing passive components and improving microelectronic applications. Hence, high dielectric permittivity (ε_r') and low dielectric loss (tan δ) values are the main requirements for any dielectric substance used in the creation of miniature electronic devices. Among various high-temperature dielectric materials, the $CaCu_3Ti_4O_{12}$ (CCTO) has gained a lot of attention from its 1st discovery by A.P. Ramirez *et. al.*[1] due to its high dielectric constant ~ (10^4 to 10^5) at nearly room temperature in the frequency range low frequency (100 Hz) to 1MHz, and it exhibits its potential applications in capacitor-based devices. The physics behind the reported gigantic dielectric effect in the perovskite-related oxide $CaCu_3Ti_4O_{12}$ was inferred and explained from optical conductivity studies of this material by C. C. Homes *et.al*.[2] Pure $CaCu_3Ti_4O_{12}$ was successfully prepared by sol-gel process using glycine-assisted nitrates solution at a low calcination temperature and short reaction time of 760°C for 4 h by P. Thongbai *et. al.* and achieved the dielectric constant 3045 at room temperature.[3] The $CaCu_3Ti_4O_{12}$ ceramic was prepared by sol-gel auto combustion process using citric acid as a chelating reagent, and its gigantic dielectric properties with low loss tangent were observed by K. Prompa *et.al.*[4] The combined effects of localized charge carriers (polarons) and conductive charge carriers in $CaCu_3Ti_4O_{12}$ were used by L. Liu *et.al.* to understand its permittivity measured at different

frequencies over a broad temperature range.[5] Using a wet-chemical combustion process, CCTO ceramic powders were successfully synthesized by J. Boonlakhorn *et.al.*, and a thorough investigation was carried out into the phase formation, microstructure, giant dielectric response ($\sim 10^3$–10^4 with a very low $\tan\delta$ of ~ 0.03–0.11 at 1 kHz), and its nonlinear electrical characteristics.[6] The exceptional dielectric properties of polyimide (PI) embedded with $CaCu_3Ti_4O_{12}$(CCTO)/Ag nanoparticles (CCTO@Ag) were reported by Y. Yang *et.al*.[7] The enhanced dielectric characteristics and voltage-current nonlinearity of solid-state reaction-prepared nickel-doped $CaCu_3Ti_4O_{12}$ (CCNTO) ceramics were examined by J. Wang *et.al*.[8] The impact of Zinc doping on the electrical and dielectric properties of CCTO compound prepared by solid state synthesis route was investigated by M. Slaoui *et. al*.[9] There are several other papers on the synthesis of CCTO compounds by different routes, various doping, and studies on their impedance and dielectric properties at low temperature to 573 K. However, its overall impedance, dielectric, conductivity, and modulus study at room temperature to extremely high temperatures up to 773K has not yet been observed. The extreme high temperature dielectric and impedance analysis is very crucial in modern technology to store and release electrical energy in high power electronics, which covers a variety of harsh environment applications in electric vehicle inverters, aerospace and avionics circuits, and oil & gas downhole sensors.

The complex double perovskite CCTO exhibits a giant dielectric constant ($\varepsilon_r \sim 10^4$ to 10^5), and it is nearly constant from low temperature (100 K) to 500 K. Due to the octahedral tilt distortion brought on by size mismatch and the characteristics of the A-sites, CCTO exhibits a perovskite-like structure that is derived from the cubic perovskite (ABO_3). Three-quarters of the sites in the TiO_6 octahedral structure have square-planar coordination and are occupied by Jahn–Teller distorted Cu^{2+} ions due to the size difference between the Ca^{2+} and Cu^{2+} ions. So far, several synthesis protocols have been documented to prepare CCTO nanoparticles or ceramics. The synthesis techniques have control over the morphology, phase purity, and particle size, all of which significantly influence the properties of CCTO and its applications. Different synthesis process such as, solid state synthesis,[10,11] sol-gel method,[12,13] co-precipitation,[14] wet-chemical method,[15] pyrolysis,[16] microwave heating,[17] polymeric precursor route,[18] and other routes have been used to synthesized CCTO but a sustainable alternatives over all those techniques is the green synthesis route which usually uses biological templates, fruit or plant extracts, or biopolymers to create CCTO nanoparticles or ceramics at lower temperatures and with less of an

adverse effect on the environment. Therefore, we have followed the green synthesis route to prepare the CCTO, which is eco-conscious, cost-effective, scalable, and capable of producing homogeneous fine powders with improved dielectric responses.[19] The prime novelty of our present work is to synthesize CCTO by a sustainable and energy-efficient green synthesis route and investigate the thermal reliability of ε_r and loss tangent (tan δ) at extremely high temperatures for its commercial usage in harsh environments by the high-temperature impedance and dielectric study.

In this research, the polycrystalline CCTO ceramic was prepared by green synthesis route using oxalate precursor and its ac electrical properties i.e. impedance, dielectric constant & loss, conductivity, and modulus spectroscopy was investigated in a wide frequency window 100 Hz to 1 MHz at temperatures ranging from 308 K to 773 K. It ensure that materials are appropriate for the harsh circumstances found in the actual world by exposing important conduction pathways, activation energies, bulk dielectric relaxation, grain and grain boundary effect, and interface behaviours that are not visible at ambient temperature.

2. Experimental Methods:

2.1. Synthesis of $CaCu_3Ti_4O_{12}$: Titanium (III) chloride solution 10-15% $TiCl_3$ basis, Sigma-Aldrich), calcium chloride ($CaCl_2$) (Sigma-Aldrich), and Copper (II) chloride ($CuCl_2$) (Sigma-Aldrich) were used with their stoichiometric ratios without any further purifications. Instead of toxic chelating reagents, we have used a mixture of aloe vera and star fruit juice, and the acidic jelly nature helps to form a very good sol-gel for auto-combustion. A thick aloe vera leaf and two ripe star-fruits (carambola fruits) were harvested and washed properly with normal water. The aloe vera juice was collected, washed, and blended in a grinder to get a uniform thick gel. The star fruits were also crushed in a grinder, and the juice was extracted by using a clear cloth. After centrifuging the collected juice for 20 minutes at 3000 rpm, the supernatant was filtered and collected. Then, both solutions were mixed properly by magnetic stirring and stored in a freezer for later use. For the preparation of 10 gm. CCTO powder samples, stoichiometric amounts of $TiCl_3$ were dissolved in 100 mL of distilled water in one container, and stoichiometric amounts of $CaCl_2$ and $CuCl_2$ were dissolved in 100 mL of distilled water in another container. Then both solution were mixed properly and 100 ml. of the extracted juice was poured in the chloride solutions.

The resultant solutions were mixed properly by magnetic stirring at 80 °C for 2 hours, and then inserted in a muffle furnace and maintained at a temperature of 300 °C for auto combustion. The final product was collected and ground well in agate mortar for 2 hours, and calcined at a temperature of 900 °C in a muffle furnace. The CCTO pellets (diameter 10 mm and thickness 1.5 mm) were prepared and calcined again at 1000 °C for 6 hours for temperature-dependent dielectric measurements.

2.2. Experimental techniques: The X-ray diffraction (XRD) measurements of CCTO were carried out by a multipurpose XRD system (RIGAKU, JAPAN & ULTIMA-IV) using Cu-kα source (λ=1.54 Å) for its phase determination in the range of 2θ between 20° and 80°, step sizes 0.001°, and scan rates 5°/min, respectively. The Raman spectroscopy of our as-prepared samples was performed to analyze vibrational properties by a PL micro Raman spectrometer (WiTec Germany, Alpha 300R) in the range of wavenumber 400 to 700 cm^{-1} using excitation wavelength (λ_{ex}) 532 nm. To examine the microstructural and morphological characterizations of CCTO pellet samples, the scanning electron microscopy (SEM) images and elemental compositions were obtained by JEOL JSM-6480 LV, EDS: Oxford Instruments equipped with energy-dispersive X-ray spectroscopy (EDS). The impedance, dielectric, and conductivity spectra measurements were performed by Hioki-IM3570 LCR meter cum impedance analyzer attached with a high temperature set-up from room temperature to 873 K and an ac frequency window 100 Hz to 1MHz.

3. Results & Discussion:

To confirm the phase pure crystalline nature, impurity detection, and other crystallographic information, the XRD pattern of the CCTO pellet sample is shown in **Figure 1**a. All diffraction peaks are well indexed to cubic body-centered perovskite structures with highly symmetric space group *Im-3* (JCPDS Card No. 75-2188)[20–22], and all experimental peaks are perfectly aligned with reference data, confirming the formation of pure CCTO structure without any impurity phases. The peak intensities are narrow and sharp, indicating that the sample has high quality and good crystallinity. The refinement pattern in **Figure 1**a demonstrates a high degree of agreement between the simulated and experimental relative intensities, as indicated by low χ^2 values~1.53. The following important structural insights were obtained from this refinement process, which involved iteratively modifying the structural model to minimize the difference between the calculated and observed diffraction patterns: the refined lattice parameters converged to the *Im-3*

space group and the refinement consistently converged to lattice parameters a = b = c=7.396 Å and α = β = γ = 90°;[23] and the refinement showed excellent agreement between the calculated and observed diffraction patterns by R_{wp}~6.3, and R_{exp}~5.05. The output structural parameters, Wyckoff position, and fractional co-ordinates are shown in **Table 1**.

Table 1. The atomic sites, Wyckoff position, and fractional co-ordinates of CCTO after Rietveld refinement[24]

Atoms	**Wyckoff position**	**Atomic co-ordinates**			**Occupancy (Occ.)**	**Isotropic displacement factor (U)**
		x	**y**	**z**		
Ca	2a	0	0	0	1	0.0096
Cu	6b	0.5	0	0	0.99998	0.0096
Ti	8c	0.25	0.25	0.25	0.99998	0.0096
O	24g	0.303	0.179	0	1.00006	0.0096

The Raman spectra of CCTO are very characteristic and extensively studied in order to comprehend its dielectric behaviour, lattice dynamics, and local distortions. **Figure 1**b illustrates the three most anticipated Raman active modes by polarized Raman studies of as-prepared CCTO (space group *Im-3*) in the range between 400-700 cm^{-1}, and it exhibits three distinct peaks around 450 cm^{-1},515 cm^{-1}, and 577 cm^{-1}, which well correspond to the previous results.[25–27] The Raman peaks at 450 cm^{-1} is associated to $A_g(1)$ and $F_g(2)$ modes, and another two peaks at 515 cm^{-1}, and 577 cm^{-1} are corresponds to $A_g(2)$ and $F_g(3)$ Raman actives modes, respectively. The modes A_g (1&2) and $F_g(2)$ originated due to lattice vibrations of TiO_6 octahedra, and $F_g(3)$ reflects the vibrations due to -O-Ti-O symmetrical bending and symmetric and antisymmetric Ti-O stretching bonds, respectively. The unit cell crystal structure of CCTO is also depicted in **Figure 1**c&d by polyhedral and ball & stick representation, obtained from the output crystallographic information file (CIF) after Rietveld refinement. The CCTO has a pseudo-cubic perovskite structure, especially a 1:3 A-site ordered perovskite having formula $A'A'''_3B_4O_{12}$ (where A'=Ca, and A'''=Cu).[28–30] A basic perovskite with A-site order is shown in the unit cell, with smaller Cu^{2+} ions at the unusual square-planar coordination with oxygen (Jahn-Teller distortion effect) and

larger Ca^{2+} ions at the A' site 12-fold coordinated at the centre and corners of the large cuboctahedron. The Ti^{4+} occupies B sites in the nearly regular TiO_6 octahedra, and O^{2-} forms the TiO_6 octahedra and Cu-O squares. The peculiar Cu^{2+} square-planar environment and the tilting and distortion of TiO_6 octahedra are essential for the enormous dielectric constant of CCTO.

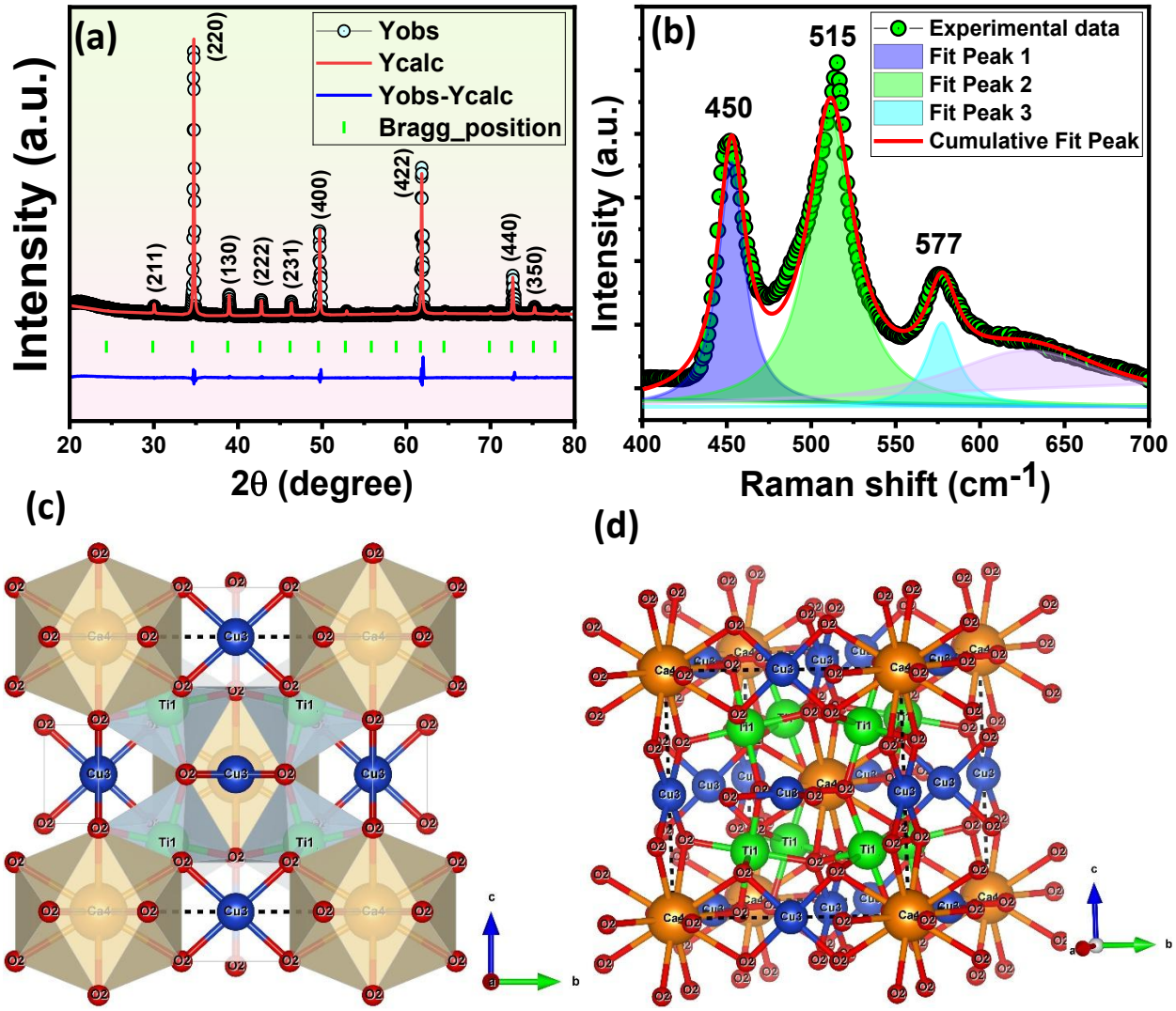

***Figure 1**: (a) The Rietveld refinement of X-ray diffraction pattern, (b) Room temperatures Raman spectra, and unit cell crystal structures (c) by polyhedral, (d) ball & stick representation of $CaCu_3Ti_4O_{12}$.*

The high-resolution scanning electron microscopy (SEM) images of CCTO pellets sintered at 1000°C for the entire dielectric and electrical transport properties are illustrated in **Figure 2**. Uniform, dense, and well-sintered microstructure of CCTO pellet at different magnification scales of 200 µm, 50 µm, 10 µm, and 5 µm are featured in **Figure 2**a-d, respectively. The well-sintered

microstructure of the CCTO pellet reveals the evolving grain connectivity, densification, and less porosity, which influences the dielectric properties significantly. The EDX (energy-dispersive X-ray) spectra of CCTO with their elemental weight (%) and atomic percentages (%) are also demonstrated in **Figure 2**e. From the atomic percentages value, it is clear that the Ca, Cu, Ti, and O follow a balanced stoichiometric ratio Ca:Cu:Ti:O=1:3:4:12 and well corresponds to the theoretical EDX composition.

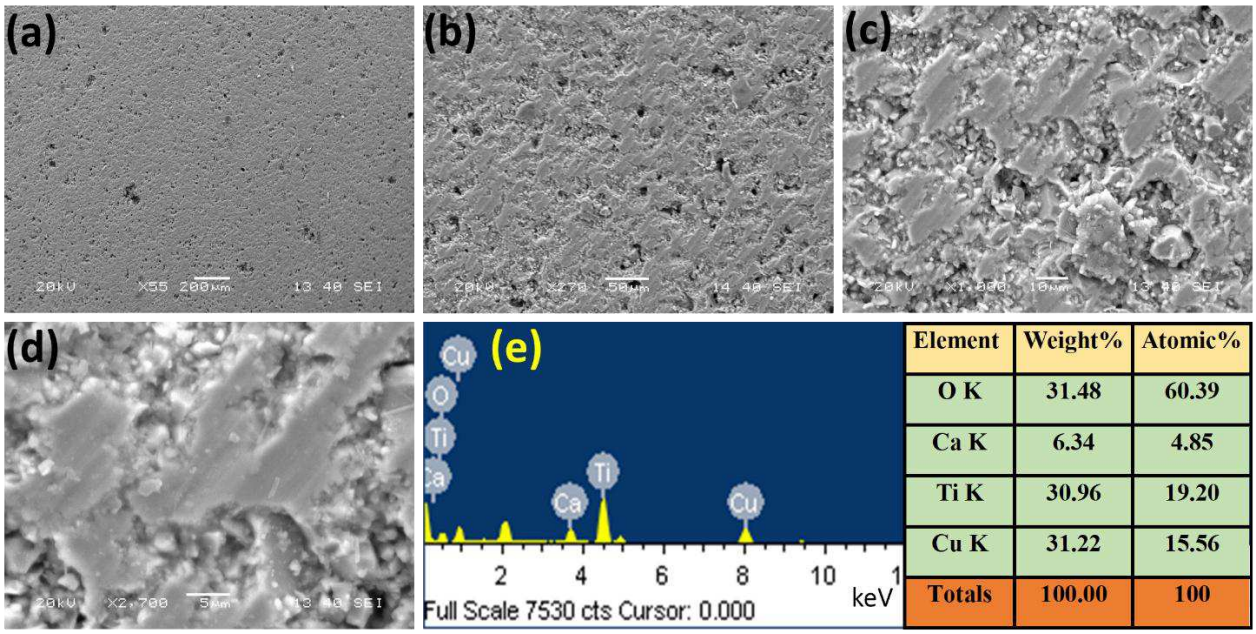

Element	Weight%	Atomic%
O K	31.48	60.39
Ca K	6.34	4.85
Ti K	30.96	19.20
Cu K	31.22	15.56
Totals	100.00	100

Figure 2: *The high-resolution scanning electron microscopy (SEM) images of the sintered $CaCu_3Ti_4O_{12}$ pellet sample for dielectric measurements at different magnification scales of (a) 200 µm, (b) 50 µm, (c) 10 µm, (d) 5 µm, and (e) the energy dispersive X-ray (EDX) pattern with the elemental weight and atomic percentages.*

Impedance spectroscopy is one of the important tools to explain dielectric relaxation and conduction mechanism, divulges the grain, grain boundary, and electrode effect, provides activation energy of the charge carriers, and enables accurate dielectric constant measurements over frequency and temperature. The real (Z') and imaginary impedance (Z'') were determined by using the formula, $Z' = Z\cos\theta$, and $Z'' = Z\sin\theta$, where θ is the phase angle.[31,32] At lower frequencies, the real part of impedance (Z') of CCTO in **Figure 3**a typically declines with increasing frequency before levelling off at higher frequencies, and it indicates an increase in AC conductivity with temperature and frequency. This behaviour is typical in high dielectric materials with high internal resistance, which results in a stable impedance value because the charge carriers

are unable to react to the fast-changing electric field at very high frequencies.[33] The observed high value of Z' at lower frequency and temperature in CCTO indicates the presence of space charge polarization. Furthermore, it was discovered that the value of Z' merged together for all temperatures at higher frequency, becoming independent of both frequency and temperature, indicating a potential release of space charge at this time. **Figure 3**b illustrates the variation of the imaginary part of impedance (Z") with frequency at various temperatures, and the appearance of relaxation peaks is clearly noticeable at higher temperatures, and it later shifted to the higher frequency region for different higher temperatures. A temperature-dependent relaxation process, potentially a modified non-Debye type relaxation in the CCTO system, is indicated by the shift in the peak position with temperature, similar to other ceramic oxide systems.[34,35] An ideal equivalent electrical circuit made up of combinations of resistance (R) and capacitance (C) is typically used to represent the impedance data in order to assess it and correlate microstructure and electrical characteristics. In most cases, the polycrystalline materials exhibit both grain, grain-boundary, and electrode ceramic interface impedances, and the complex impedance (Z^*) is represented by[36,37]

$$Z^* = Z' + iZ'' = \frac{1}{\frac{1}{R_g}+i\omega C_g} + \frac{1}{\frac{1}{R_{gb}}+i\omega C_{gb}+A_0(i\omega)^n} + \frac{1}{\frac{1}{R_{cl}}+i\omega C_{cl}} \dots (1)$$

where,

$$Z' = \frac{R_g}{1+(\omega R_g C_g)^2} + \frac{(1+A\omega^n)^2}{(1+A\omega^n)^2+(\omega R_{gb}C_{gb}+B\omega^n)^2} + \frac{R_{cl}}{1+(\omega R_{cl}C_{cl})^2} \dots (2)$$

and,

$$Z'' = \frac{\omega {R_g}^2 C_g}{1+(\omega R_g C_g)^2} + R_{gb}\left[\frac{\omega R_{gb}C_{gb}+B\omega^n}{(1+A\omega^n)^2+\left(\omega R_{gb}C_{gb}+B\omega^n\right)^2}\right] + \frac{\omega {R_{cl}}^2 C_{cl}}{1+(\omega R_{cl}C_{cl})^2} \dots (3)$$

The parameters R_g, C_g, R_{gb}, and C_{gb} symbolize the grain, grain boundary resistance, and capacitances, respectively. The **Figure 3**a&b is fitted and correlated by eq^n (2&3) where A and B are the dimensionless constants $A = A_0 R_{gb}\cos\left(\frac{n\pi}{2}\right)$ and $B = A_0 R_{gb}\sin\left(\frac{n\pi}{2}\right)$. The appearance of a relaxation peak (Z''_{max}) at a characteristic frequency ($\omega_{max} = 2\pi\nu_{max}$) in the Z'' vs. frequency plot is associated with the dipolar reorientation, hopping conduction, grain boundary polarization, etc., and it also confirms the presence of space charge in the system. The peaks of imaginary impedance shift with frequency dispersion in response to temperature because thermally activated charge carrier dynamics regulate relaxation times with frequency.

The Nyquist plots (Z' vs. Z'') of CCTO are demonstrated in **Figure 3**c-f at various temperatures, 308 K to 773 K, and fitted with an equivalent network circuit model (RC)((Q)RC)(RC) using ZSIMPWIN 3.2.1 software. It is clearly noticeable that one arc of a semicircle appears in the Nyquist plot from 308 K to 473 K in the high-frequency region, which is mainly associated with the grain (bulk) response. With increasing temperature, a completely depressed semicircle appears in the Nyquist plot, which is a combination of both grain (bulk) and grain boundary contributions, 498 K-673 K. The depressed semicircle in the Nyquist plots indicates the distribution of relaxation time rather than a single relaxation time (τ), and it recommends a non-Debye type relaxation in CCTO. The equivalent circuit model was established based on the brick-layer model, considering the grain, grain boundary, and electrode-ceramic interface effect, similar to other polycrystalline materials. A polycrystalline ceramic is treated by the brick-layer model[38–40] as conducting "bricks" (grains) divided by thin insulating "mortar" (grain boundaries). Nyquist plots of CCTO and related ceramics typically display two overlapped semi-circular arcs (grain + grain boundary), which can be explained by the fact that its corresponding circuit typically consists of two parallel RC and QRC elements in series. Another RC element mainly arises due to the compelling electrode ceramic interface effect at higher temperatures. The constant phase element (Q) is known as a constant phase element, which is represented by[41,42]

$$Z_{CPE} = \frac{1}{Q(i\omega)^n} \dots (4)$$

where n is the exponent and its value is 1 for an ideal capacitor and 0 for an ideal resistor. The resistance of the material is determined by the radius of the semi-circular arc, which also offers information on a variety of conduction models at different temperatures. At extremely high temperatures from 698K to 773K in **Figure 3**f, the Nyquist plot looks truncated (cut-off) instead of showing a full arc. This is because the grain conductivity increases strongly at high temperatures, and the bulk resistance drops drastically. Additionally, high temperatures induce increased mobile carriers to collect at blocking electrodes, creating a significant interfacial polarization that dominates the low-frequency impedance response and results in the electrode–ceramic effect in Nyquist plots.[43]

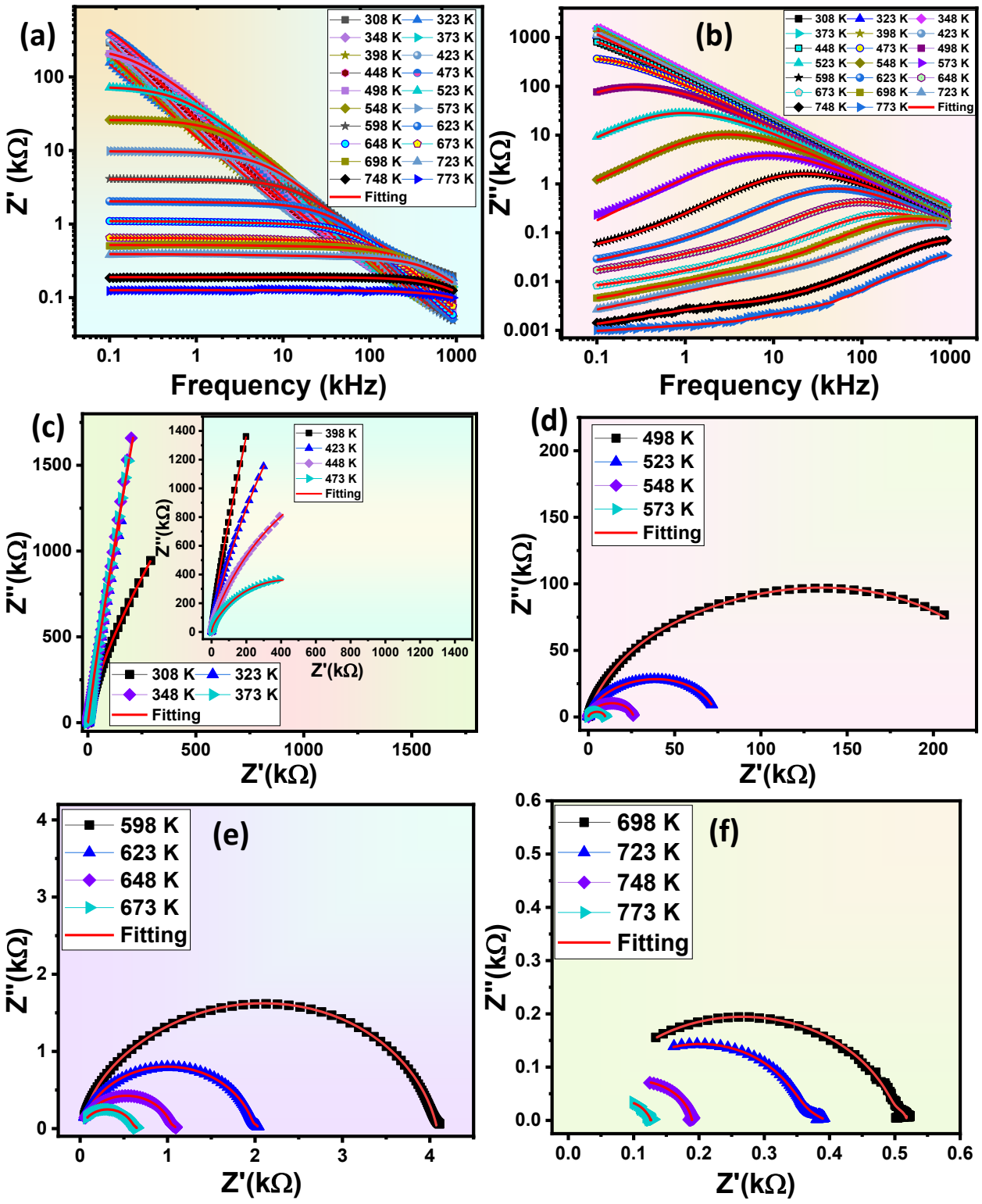

Figure 3: *The frequency dependence (a) real impedance (Z′), (b) imaginary impedance (Z″) at various temperatures. The Nyquist plots (Z′vs.Z″) at different temperatures between (c) 308 K-473 K, (d) 498 K-573 K, (e) 598 K-673 K, (f) 698 K-773 K.*

The variation of grain and grain boundary resistance (R_g, R_{gb}), and grain and grain boundary capacitance (C_g, C_{gb}) with temperatures (K) is displayed in **Figure 4**a&b, respectively. Both R_g and R_{gb} values decreases with temperatures (K) from10 kΩ and 1×10^{10} Ω to 25Ω to 30Ω form temperature 308 K to 773 K. Grain boundaries (GB) are typically more resistant because of insulating secondary phases, oxygen enrichment, or defect segregation and the grain boundary resistance drastically decreases at high temperature as trapped carriers at GBs acquire energy to overcome the barrier. In CCTO, the electrical conduction mainly occurs due to small polarons hopping of mixed valence states Ti^{3+}/Ti^{4+}, Cu^{1+}/Cu^{2+} between localized states over a barrier, and the activation energy (E_a) for grain and grain boundary was estimated using the Arrhenius equation,[14,44]

$$R(T) = R_0 \exp\left(\frac{E_a}{k_B T}\right) \ldots (5)$$

where R_0 and k_B are the pre-exponential factor and Boltzmann constant (8.617×10^{-5} eV K^{-1}), and it is illustrated in **Figure 4**a-inset. The activation energy for grain and grain boundary is determined 0.56 eV and 0.84 eV for grain and grain boundary, respectively. The activation energy for the grain boundary is higher than that of the grain, as it presents barriers to charge transport. The grain (C_g) and grain boundary capacitance (C_{gb}) with temperature (K) are depicted in **Figure 4**b, and both values diminished with temperature (K). Both C_g and C_{gb} decrease with temperature because the heat agitation decreases the polarization ability (dipolar + interfacial) of mobile carriers, which in turn diminishes effective charge storage across grains and grain boundaries. The grains (bulk) exhibit low resistance and small capacitance, and grain boundaries have high resistance and large capacitance.

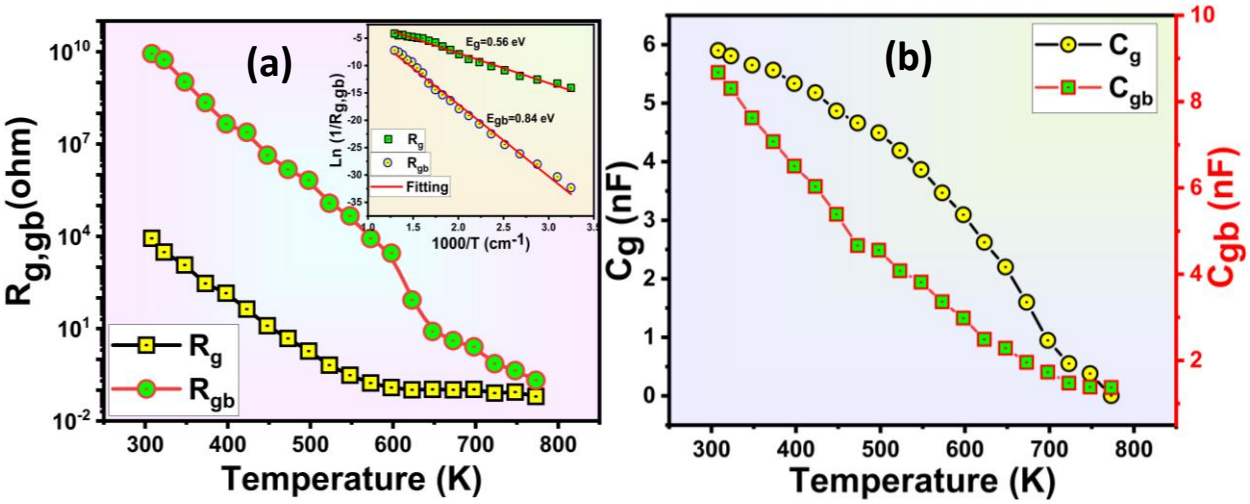

Figure 4: *The variation of (a) grain (R_g) and grain boundary resistance (R_{gb}), (b) grain (C_g) and grain boundary (C_{gb}) capacitance with temperature. The activation energy of grain (E_g) and grain boundary (E_{gb}) by Arrhenius plot is shown in the inset of Figure 4a.*

Designing CCTO-based devices for capacitors, sensors, and high-power electronics requires an understanding of the AC conduction mechanism, grain-grain boundary effects, dielectric relaxation, and thermal stability, and that information is revealed by studying the AC electrical conductivity of CCTO with temperature. In contrast to the dielectric measurement of CCTO, the ac electrical conductivity is very rarely explored. The real (σ') and imaginary conductivity (σ'') were determined from impedance data by the formula, $\sigma' = \frac{t}{A}\frac{Z'}{Z'^2+Z''^2}$ and $\sigma'' = \frac{t}{A}\frac{Z''}{Z'^2+Z''^2}$; where t and A are the thickness and area of a parallel plate capacitor. The frequency dependence σ' and σ'' plots at various temperatures from 308 K to 773 K are depicted in **Figure 5**a&b, respectively. Jonscher attempted to use the following law to describe the behaviour of AC conductivity when the applied field causes the charges to migrate,[45–47]

$$\sigma_T(\omega) = \sigma(0) + \sigma_1(\omega) = \sigma_0(dc) + B\omega^n \ \ldots (6)$$

where σ_0, B, and n are the dc conductivity, pre-exponential factor dependent on temperature, and n ($0 < n < 1$) is the frequency exponent, respectively. At low frequency, the conductivity is nearly constant (except for a few near room temperature) and independent of frequency, and it corresponds to the dc conductivity. The ac conduction is dominated by grain boundaries, which serve as insulating barriers, and long-range migration of charge carriers across the grain or grain boundary is responsible for dc conduction. At low temperatures, the charge carriers are less thermally activated, and the conduction plateau is smaller. At the high frequency region, the charge

carriers engage in short-range hopping (localized mobility) between defect states/traps (Ti^{3+}/Ti^{4+}, Cu^{2+}/Cu^{3+}) within the grain or at the interface, which leads to the dispersion in $\sigma_T(\omega)$.[48] The grain boundary effects, interfacial contributions (moisture, surface states), electrode polarization, and instrumental constraints are the principal causes of small changes in the low-frequency imaginary AC conductivity region in **Figure 5**b. Typically, they are not inherent to the bulk properties of the material. The variation of frequency exponent (n) and B with temperature (K) is delineated in **Figure 5**c. The n value remains nearly constant (~ 0.9 to 0.95) in the temperature range between 308K and 573K, and then it decreases with temperature up to 773K. In the near room temperature region, the frequency exponent reveals a quantum mechanical tunnelling conduction mechanism where the charge carriers, such as electrons or holes, tunnel across a potential barrier using quantum mechanical law rather than requiring enough thermal activation. According to the QMT model, the n value is nearly temperature independent or shows very weak temperature variation by the formula,[49,50]

$$n = 1 - \frac{4}{\ln\left(\frac{1}{\omega\tau_0}\right)} \approx 1 - \frac{4}{\ln(\omega\tau_0)} \ldots (7)$$

The parameter τ_0 represents the characteristic relaxation time (often ~10^{-12} or 10^{-13} s for localized states).

As the temperature increases enough above 573K, the tunneling of charge carriers is dominated by thermally activated hopping of charge carriers over barriers between localized states with the correlation of Coulomb interaction, barrier heights, etc. In this region, the frequency exponent decreases with the increase of the temperature, and it follows the correlated barrier hopping (CBH) conduction model. Few studies on CCTO reveal the CBH as a prime conduction mechanism and ruled out the tunneling mechanism explicitly via high field or below room temperature measurements. Therefore, it is confirmed that the conduction mechanism related to the grain boundary effect commemorated the CBH model provided by Pike, where the thermal excitation is responsible for the transfer of electrons over the barriers between two sites. The ac conductivity and the frequency exponent (n) can be expressed by,[51,52]

$$\sigma_{ac}(\omega) = \frac{\pi^3}{24} N^2 \varepsilon\varepsilon_0 \omega R_\omega^6 \ldots (8)$$

and,

$$n = 1 - \frac{6k_BT}{W_M} \ldots (9)$$

where N, R_ω, and W_M are the concentration of pure states, hopping distances, and the barrier height, respectively. The W_M value is determined by fitting the frequency exponent data with a linear fit using eq^n(9), and its value is calculated to be ~0.056 eV. The QMT predominates in CCTO at near room temperature since tunnelling is the sole practical mechanism in the absence of sufficient thermal energy in charge carriers. The temperature dependency of frequency exponent exhibits a direct shift toward CBH as the temperature rises because carriers now possess sufficient energy to hop over barriers between localized sites. The dc conductivity values were collected from the output of Jonscher's power law fitting, and the activation energy was calculated from the slope of $\mathrm{Ln}(\sigma_{dc} * \mathrm{T})$ vs. 1000/T (K^{-1}), shown in **Figure 5**d. The temperature-modified Arrhenius equation, which is used to calculate the dc activation energy (E_a),[53]

$$\sigma_{dc} * T = \sigma_0 \exp\left(-\frac{E_a}{k_B T}\right) \ldots (10)$$

and the DC activation energy for two different regions was obtained as ~ 0.51 eV (QMT) and ~0.62 eV (CBH). The dc activation energy reflects the energy required for the charge carrier (usually small polarons or defect-related carriers) to move across the insulating grain boundary of CCTO. The temperature dependence of the ac conductivity at different frequencies is displayed by a 3-dimensional (3D) graph in **Figure 5**e, which shows that the ac conductivity is more pronounced at near room temperature for different frequencies between 100Hz and 1MHz. The AC conductivity of CCTO rises with temperature because thermal energy improves the tunnelling/hopping probability of localized carriers and decreases the effective barriers at grain boundaries, resulting in more effective charge transport under an alternating electric field. The activation energy is also calculated using the Arrhenius equation,[54,55]

$$\sigma_{ac}(\omega, T) = \sigma_0(\omega) \exp\left(-\frac{E_a}{k_B T}\right) \ldots (11)$$

and it is illustrated in **Figure 5**f for different frequencies. The ac activation energy decreases from 0.4 eV to 0.24 eV as the frequency of ac field changes from 100 Hz to 1 MHz. One of the most compelling proof in favour of the (internal barrier layer capacitor model) IBLC model in CCTO (semiconducting grains + insulating GB) is this frequency dependency of E_a.

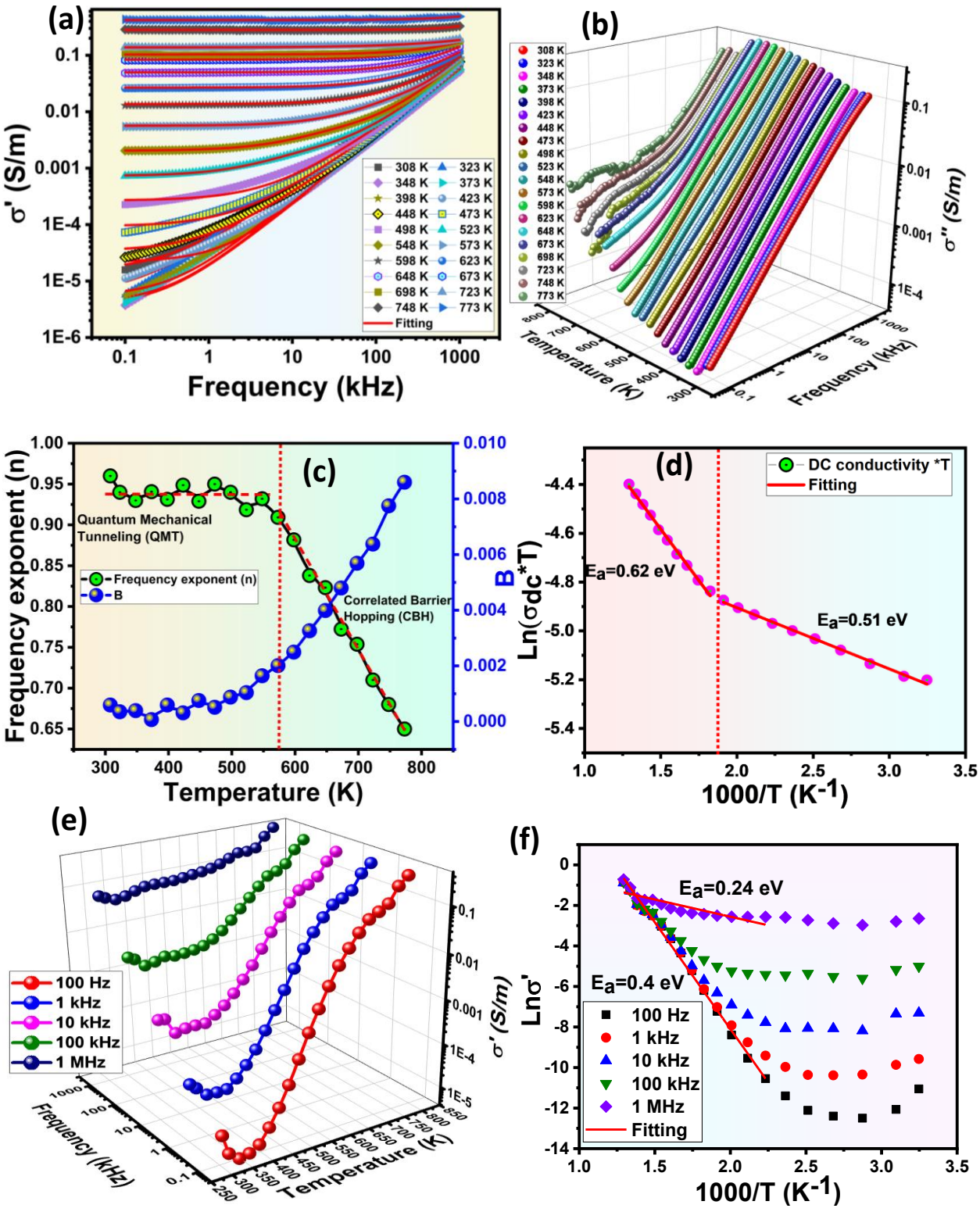

Figure 5: *The frequency-dependent (a) real ac conductivity (σ′), (b) imaginary ac conductivity (σ″) at various temperatures. (c) The variation of frequency exponent (n) and the parameter B with temperature (K), and (d) the Arrhenius plot of dc activation energy. (e) The temperature and*

frequency dependence of real ac conductivity (σ'), and (f) the Arrhenius plot of ac activation energy.

The enormous dielectric constant, conduction and relaxation mechanisms, microstructure-property relationship, and optimization guidance for capacitor and energy storage applications make the dielectric study of CCTO very crucial and significant at high temperatures. In our study, the real (ε'), imaginary dielectric constant (ε''), and dielectric loss (δ) were calculated using the formula,[56]

$$\varepsilon' = \frac{t}{\omega A \varepsilon_0} \frac{Z''}{Z'^2 + Z''^2} \ldots (12)$$

$$\varepsilon'' = \frac{t}{\omega A \varepsilon_0} \frac{Z'}{Z'^2 + Z''^2} \ldots (13)$$

$$\text{and, } \tan\delta = \frac{\varepsilon''}{\varepsilon'} \ldots (14)$$

Figure 6a&b demonstrated the frequency dispersing ε' and ε'' of CCTO at wide temperature ranges from 308K to 773K, and both values decrease with frequency. The ε' value of CCTO is extremely large ~10×10^3 in the low frequency region at room temperature 308 K, and its value increases up to ~660×10^3 at a temperature of 773 K. The high dielectric constant (ε' or ε'') at low frequency is one of the most striking features of most of the oxide materials, and the IBLC effect plays an important role in enhancing the dielectric constant in CCTO. CCTO is mainly composed of semiconducting grains with low resistance and small capacitance, and nearly insulating grain boundaries with high resistance and large capacitance. The charge carriers migrate and accumulate at the grain boundaries in the low-frequency region, and this accumulation of space charges acts in series like several internal capacitors, giving rise to the colossal dielectric constant. Additionally, the Maxwell-Wagner interfacial polarization makes a significant contribution to producing a very large dielectric response.[57] At high frequency, the charges cannot follow the fast oscillations of the external electric field, resulting in polarization drop and curtailment of both dielectric constant (ε' or ε''). The complex dielectric constant (ε^*) of CCTO is expressed as,[58,59]

$$\varepsilon^*(\omega) = \varepsilon_\infty + \frac{\varepsilon_s - \varepsilon_\infty}{1 + (i\omega\tau)^{1-\alpha}} \ldots (15)$$

The real and imaginary parts are

$$\varepsilon'(\omega) = \varepsilon_\infty + \frac{(\varepsilon_s - \varepsilon_\infty)}{2}\left[1 + \frac{1+(\omega\tau)^{1-\alpha}\cos\left(\frac{\pi(1-\alpha)}{2}\right)}{\left[\left(1+2(\omega\tau)^{(1-\alpha)}\cos\left(\frac{\pi(1-\alpha)}{2}\right)\right)+(\omega\tau)^{2(1-\alpha)}\right]^{1/2}}\right] \ldots (16)$$

$$\text{and, } \varepsilon''(\omega) = \frac{(\varepsilon_s - \varepsilon_\infty)}{2}\left[\frac{(\omega\tau)^{1-\alpha}\sin\left(\frac{\pi(1-\alpha)}{2}\right)}{\left[\left(1+2(\omega\tau)^{(1-\alpha)}\cos\left(\frac{\pi(1-\alpha)}{2}\right)\right)+(\omega\tau)^{2(1-\alpha)}\right]^{1/2}}\right] \ldots (17)$$

Figure 6a is fitted by eq^{n}(16) and the parameters ε_s and ε_∞ represent low and high frequency dielectric constant, and τ, ω, α are the characteristics relaxation time, angular frequency (= $2\pi\nu$), and Cole-Cole broadening parameters ($0 \leq \alpha < 1$) or distribution of relaxation time. The variation of Cole-Cole parameter (α) with temperature (K) is portrayed in **Figure 6**c, and its value also makes a downturn from 0.85 to 0.19 with temperature evolution. In materials like CCTO, the Cole–Cole parameter (α >0) is crucial because it gauges the extent of non-Debye behaviour and sheds light on conduction mechanisms, relaxation dynamics, and microstructural disorder.[60] The physical processes at the grains and grain boundaries are connected to experimental dielectric data. **Figure 6**d depicted the temperature dependence real dielectric constant (ε') at different frequency from 100 Hz to 1 MHz and ε' start increasing rapidly after 500 K. At high temperatures, Ti^{3+}/Ti^{4+}, and Cu^{2+}/Cu^{3+} states releases more carriers (polarons) which can move more easily between localized states which in turn boost up space charge polarization at grain boundary and upsurge the dielectric constant. The variation of dielectric loss (δ) with frequency is illustrated in **Figure 6**e, which shows a decreasing trend with frequency at various temperatures. Maxwell-Wagner type interfacial polarization causes significant dissipation in the low frequency region, and the leakage current and electrode effect dominate. As the frequency increases, interfacial polarization as well as loss decrease, showing a weak relaxation plateau, which is also evidence of a non-Debye relaxation process.[61] At the high frequency region, the influence of electronic and ionic polarization starts contributing more, and the space charge or dipolar contribution diminishes. The loss lessened gradually and tended to merge into a constant value. The temperature-dependent loss at various frequencies from 100 Hz to 1 MHz is highlighted in **Figure 6**f, where high temperature has a significant impact on loss at different frequencies. High temperature induces the IBLC, Maxwell-Wagner polarization, and leakage effect in CCTO, which results in higher loss in CCTO.

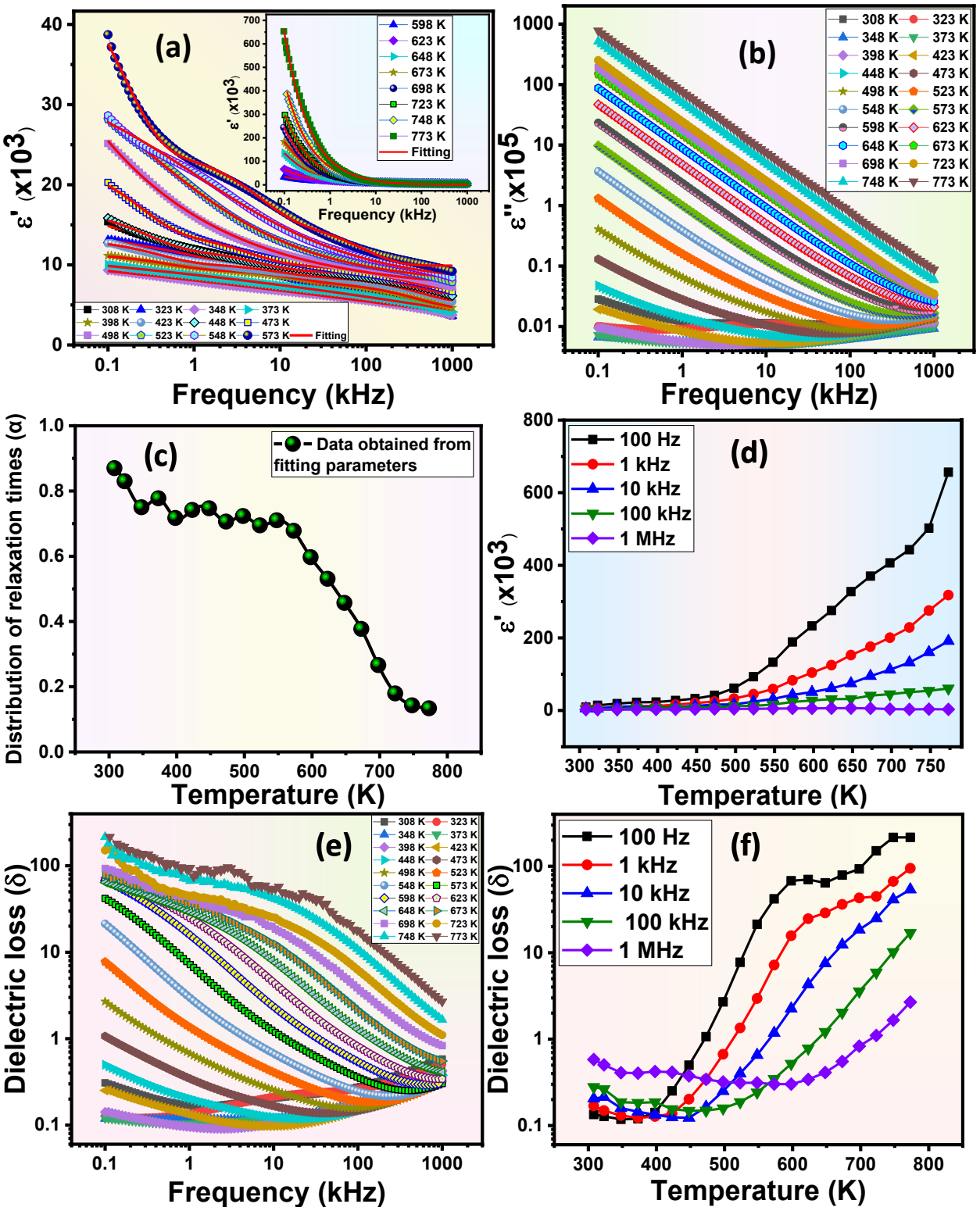

Figure 6: *The frequency dispersing (a) real dielectric permittivity (ε′), (b) imaginary dielectric permittivity (ε″) at different temperatures from 308 K to 773 K. (c) The distribution of Cole-Cole parameters or distributions of relaxation times with temperatures. The real dielectric permittivity*

(ε') vs. temperature at different frequencies. (e&f) The frequency and temperature dependence of dielectric loss (δ) of $CaCu_3Ti_4O_{12}$.

The modulus spectra in CCTO are very important because they separate the grain and grain boundary contributions and minimize the electrode effect, focus on the capacitance-related process, and give a complementary and clearer view of relaxation dynamics.[62] The real (M') and imaginary modulus (M'') are formulated from the real and imaginary dielectric permittivity, and these are expressed as follows,

$$M' = \frac{\varepsilon'}{\varepsilon'^2 + \varepsilon''^2} \ldots (18)$$

$$M'' = \frac{\varepsilon''}{\varepsilon'^2 + \varepsilon''^2} \ldots (19)$$

The frequency-dependent M' and M'' spectra at various temperatures from 308 K to 773 K are emphasized in **Figure 7**a&b, respectively. Asymptotic variation and broad, dispersed M' relaxation in CCTO is observed, which possibly arises due to structural disorder, defects, change in oxidation states Cu^{2+}/Cu^{3+}, Ti^{3+}/Ti^{4+}, and grain boundary effect at high temperature. Few capricious relaxation peaks at high temperature are a signature of microstructural inhomogeneity or measurement-related factors rather than intrinsic theory. The imaginary part of the electric modulus in **Figure 7**b for various temperatures has been fitted using an approximate frequency representation of the Bergman-proposed Kohlrausch–Williams–Watts (KWW) function,[63,64]

$$M'' = \frac{M''_{1max}}{\left((1-\beta_1)+\left(\frac{\beta_1}{1+\beta_1}\right)\right)\left[\left(\frac{\omega_{1max}}{\omega}\right)+\left(\frac{\omega}{\omega_{1max}}\right)^{\beta_1}\right]} + \frac{M''_{2max}}{\left((1-\beta_2)+\left(\frac{\beta_2}{1+\beta_2}\right)\right)\left[\left(\frac{\omega_{2max}}{\omega}\right)+\left(\frac{\omega}{\omega_{2max}}\right)^{\beta_2}\right]} \ldots (20)$$

where, M''_{max} and ω_{max} are the imaginary modulus peaks and angular frequency maximum for the grain and grain boundary, respectively. The exponent β is known as the empirical Kohlrausch function that appears in the range ($0<\beta<1$). The grain and grain boundary contribution looks imbricated together in broad relaxation peaks, and the mutual dependency of M''_{1max} and M''_{2max} was taken care of during perfect fitting. The low-frequency M'' is associated with the grain boundary relaxation, and it overlapped with high-frequency grain relaxation peaks. In CCTO, the mixed valence states (Cu^{2+}/Cu^{3+}, Ti^{3+}/Ti^{4+}) and inhomogeneous microstructure contribute broadened and asymmetric relaxation peaks and reconfirm the non-Debye type relaxation

process.[65] The M'' peaks also shifted towards higher frequency with temperature, following an Arrhenius-type activation energy. The Cole-Cole plot of modulus ($\mathrm{M'vs.M''}$) is also interpreted in **Figure 7**c, and the depressed arc/non-ideal semicircle suggested a temperature-dependent hopping mechanism for electric conduction (charge transport) in the system and non-Debye type dielectric relaxation by its behaviour. The centre of all arcs is depressed below the real axis, which reconfirmed the Cole-Cole broadening parameter ($\alpha > 0$). The grain and grain boundary activation energy is determined from the peak frequency (ω_m) using [66]

$$\omega_m = \omega_0 \exp\left(-\frac{E_a}{k_B T}\right) \ldots (21)$$

where ω_m is the peak relaxation frequency and k_B is the Boltzmann constant. The activation energy for grain and grain boundary was obtained as ~ 0.54 eV and 0.81 eV for grain and grain boundary, respectively, which corresponds to the impedance data.

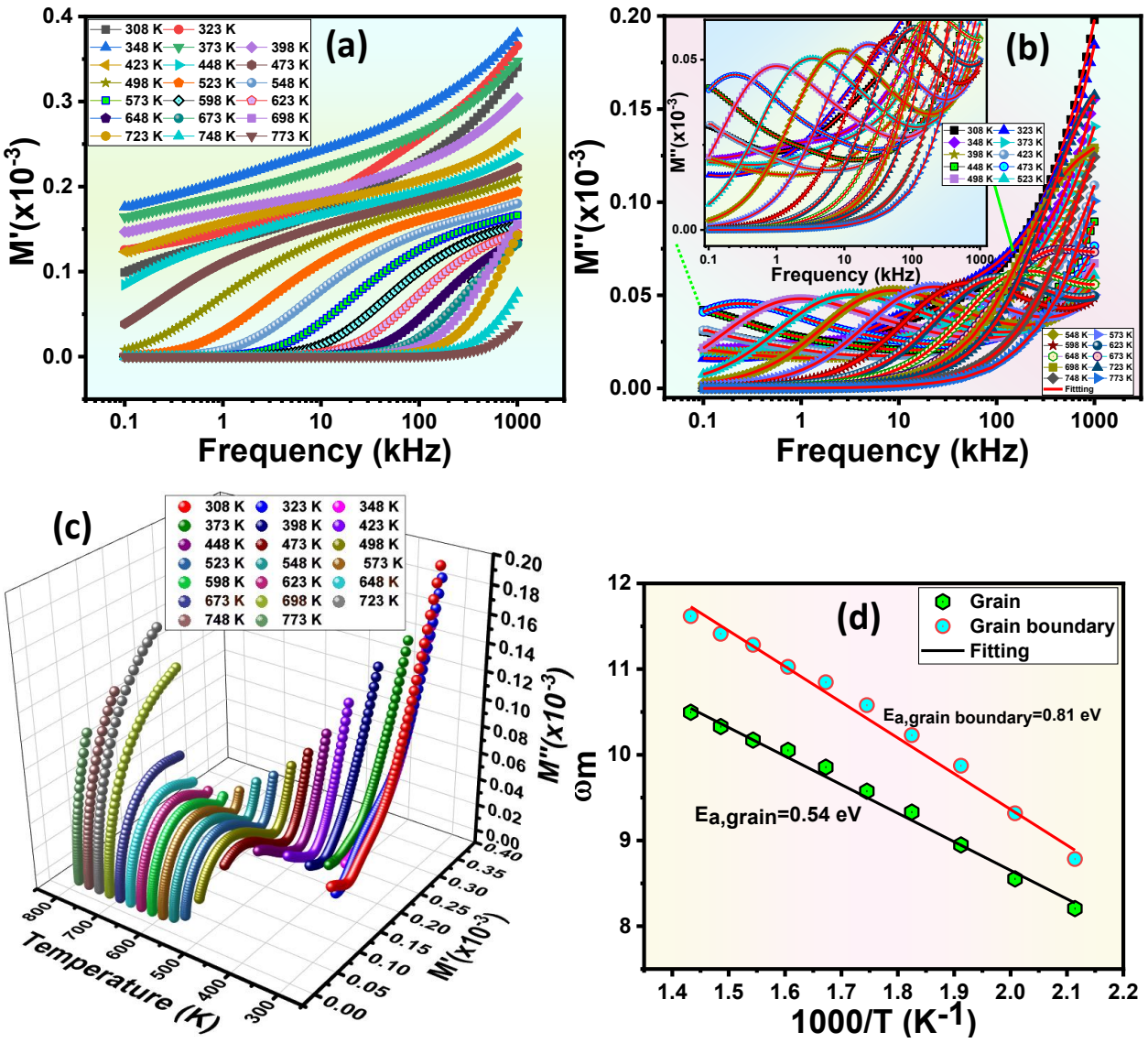

Figure 7: *The variation of (a) real modulus (M′), (b) imaginary modulus (M″) with frequency at various observed temperatures. (c) The Cole-Cole plot of modulus (M′ vs. M″), (d) The Arrhenius plots of activation energy for grain and grain boundary.*

4. Conclusion:

In summary, the CCTO was prepared by a unique green synthesis route, and its frequency (100 Hz-MHz) dependent conductivity and dielectric properties were investigated over a wide temperature region from 308 K to 773 K. The Rietveld refinement of the XRD pattern reveals a polycrystalline nature and perfect intensity peak matching with standard cubic CCTO (space group *Im-3*), and no significant secondary phases or residual precursors were detected. The A_g and F_g modes in Raman spectra confirm the vibrational modes of TiO_6 octahedra, O-Ti-O symmetrical bending, and Cu-O bonds, which are crucial for dielectric properties. The true stoichiometrical

ratio of CCTO $Ca:Cu:Ti:O = 1:3:4:12$ is corroborated by the atomic weight percentage from EDX spectra and elemental analysis. The low-frequency arc in the Nyquist plot ($Z' \; vs. \; Z''$) is related to a highly resistive grain boundary, and it dominates the giant dielectric permittivity of CCTO due to blocking charge carriers. The giant dielectric constant (~1×10^4 @ 100 Hz and 308 K) originated due to **the** internal barrier layer capacitor (IBLC) model, and non-Debye type dielectric relaxation is observed. The activation energy (E_a) for grain and grain boundary was determined to be ~0.54 eV and ~0.81 eV from the impedance plot, which well corresponds to modulus analysis. The ac conductivity of CCTO is strongly frequency and temperature-dependent and follows Jonscher's power law. The variation of frequency exponent (n) with temperature indicates a transition of quantum mechanical tunneling (QMT) at low temperature to correlated barrier hopping (CBH) conduction mechanism at high temperature. The dc activation energy was estimated to be ~0.51 eV for QMT and ~0.62 eV for the CBH model by using the Arrhenius equation. The dielectric permittivity is high in the low frequency region and decreases with increasing frequency, reflecting thermally activated interfacial polarization (Maxwell-Wagner). The dielectric spectra are correlated by the modified Cole-Cole equation, and the Cole–Cole parameter ($\alpha > 0$) measures the deviation from ideal Debye behaviour. The modulus formalism confirms the IBLC mechanism in CCTO and complements impedance data by emphasizing the significance of localized polaron dynamics and grain boundary relaxation, which makes it a suitable material for high-permittivity capacitors and energy storage applications.

Acknowledgement

We would like to acknowledge the faculty and staff of the Department of Physics, REVA University, and Manipal University, Jaipur, for their support in carrying out this project. The author, Dr. SK, wants to acknowledge Mr. Vignesh. P from REVA University for his help in this project.

Declaration of competing interests

The authors declare that they have no known competing financial interests or personal relationships that could have appeared to influence the work reported in this paper.

Funding declaration statement

The author received no funding for this work.

Data availability

Data is provided within the manuscript.

References

1. Ramirez, A. P. *et al.* Giant dielectric constant response in a copper-titanate. *Solid State Commun.* **115**, 217–220 (2000).
2. Homes, C. C., Vogt, T., Shapiro, S. M., Wakimoto, S. & Ramirez, A. P. Optical Response of High-Dielectric-Constant Perovskite-Related Oxide. *Science* **293**, 673–676 (2001).
3. Thongbai, P., Yamwong, T., Maensiri, S., Amornkitbamrung, V. & Chindaprasirt, P. Improved Dielectric and Nonlinear Electrical Properties of Fine-Grained $CaCu_3$ Ti_4 O_{12} Ceramics Prepared by a Glycine-Nitrate Process. *J. Am. Ceram. Soc.* **97**, 1785–1790 (2014).
4. Prompa, K., Swatsitang, E. & Putjuso, T. Very low loss tangent and giant dielectric properties of CaCu3Ti4O12 ceramics prepared by the sol–gel process. *J. Mater. Sci. Mater. Electron.* **28**, 15033–15042 (2017).
5. Liu, L. *et al.* Localized polarons and conductive charge carriers: Understanding CaCu 3 Ti 4 O 12 over a broad temperature range. *Phys. Rev. B* **99**, 094110 (2019).
6. Boonlakhorn, J., Kidkhunthod, P. & Thongbai, P. Investigation of the dielectric properties and nonlinear electrical response of CaCu3Ti4O12 ceramics prepared by a chemical combustion method. *J. Mater. Sci. Mater. Electron.* **31**, 4511–4519 (2020).
7. Yang, Y. *et al.* High performance of polyimide/$CaCu_3$ Ti_4 O_{12} @Ag hybrid films with enhanced dielectric permittivity and low dielectric loss. *J. Mater. Chem. A* **3**, 4916–4921 (2015).
8. Wang, J., Lu, Z., Deng, T., Zhong, C. & Chen, Z. Improved dielectric properties in A′-site nickel-doped $CaCu_3$ Ti_4 O_{12} ceramics. *J. Am. Ceram. Soc.* **100**, 4021–4032 (2017).

9. Slaoui, M. *et al.* Effect of Zinc Doping on the Electrical and DielectricProperties of CCTO Compound Synthesized by Solid-State Method. *Asian J. Chem.* **33**, 2000–2006 (2021).
10. Ramírez, M. A., Bueno, P. R., Varela, J. A. & Longo, E. Non-Ohmic and dielectric properties of a Ca2Cu2Ti4O12 polycrystalline system. *Appl. Phys. Lett.* **89**, 212102 (2006).
11. Subramanian, M. A., Li, D., Duan, N., Reisner, B. A. & Sleight, A. W. High Dielectric Constant in ACu3Ti4O12 and ACu3Ti3FeO12 Phases. *J. Solid State Chem.* **151**, 323–325 (2000).
12. Zhang, J. *et al.* The dielectric properties of CCTO ceramics prepared via different quick quenching methods. *Mater. Res. Bull.* **115**, 49–54 (2019).
13. Sun, L. *et al.* Sol–gel synthesized pure CaCu3Ti4O12 with very low dielectric loss and high dielectric constant. *Ceram. Int.* **41**, 13486–13492 (2015).
14. Lu, J., Wang, D. & Zhao, C. CaCu3Ti4O12 ceramics from basic co-precipitation (BCP) method: Fabrication and properties. *J. Alloys Compd.* **509**, 3103–3107 (2011).
15. Liu, J., Smith, R. W. & Mei, W.-N. Synthesis of the Giant Dielectric Constant Material $CaCu_3 Ti_4 O_{12}$ by Wet-Chemistry Methods. *Chem. Mater.* **19**, 6020–6024 (2007).
16. Liu, J. *et al.* $CaCu_3 Ti_4 O_{12}$: Low-Temperature Synthesis by Pyrolysis of an Organic Solution. *Chem. Mater.* **18**, 3878–3882 (2006).
17. Yu, H., Liu, H., Luo, D. & Cao, M. Microwave synthesis of high dielectric constant CaCu3Ti4O12. *J. Mater. Process. Technol.* **208**, 145–148 (2008).
18. Jha, P., Arora, P. & Ganguli, A. K. Polymeric citrate precursor route to the synthesis of the high dielectric constant oxide, CaCu3Ti4O12. *Mater. Lett.* **57**, 2443–2446 (2003).

19. Etape, E. P. *et al.* Nanosize $CaCu_3$ Ti_4 O_{12} Green Synthesis and Characterization of a Precursor Oxalate Obtained from *Averrhoa carambola* Fruit Juice and Its Thermal Decomposition to the Perovskite. *J. Nanomater.* **2020**, 1–7 (2020).
20. Kumari, N., Meena, S., Rathore, D., Singhal, R. & Dwivedi, U. K. Study of dielectric properties of CaCu3Ti4O12 synthesized via different routes: Effect of sintering temperature. *Ceram. Int.* **49**, 2549–2556 (2023).
21. Sun, L. *et al.* Sol–gel synthesized pure CaCu3Ti4O12 with very low dielectric loss and high dielectric constant. *Ceram. Int.* **41**, 13486–13492 (2015).
22. Maddu, A., Yulwan, H., Sofian, I., Sulaeman, A. S. & Putro, P. A. Synthesis of CaCu3Ti4O12 utilizing eggshell waste as a calcium source: Structure, morphology, and dielectric properties. *J. Met. Mater. Miner.* **32**, 80–85 (2022).
23. Kotb, H. M., Ahmad, M. M., Alshoaibi, A. & Yamada, K. Dielectric Response and Structural Analysis of (A3+, Nb5+) Cosubstituted CaCu3Ti4O12 Ceramics (A: Al and Bi). *Materials* **13**, 5822 (2020).
24. Ahmadipour, M., Ain, M. F. & Ahmad, Z. A. A Short Review on Copper Calcium Titanate (CCTO) Electroceramic: Synthesis, Dielectric Properties, Film Deposition, and Sensing Application. *Nano-Micro Lett.* **8**, 291–311 (2016).
25. Saîd, S., Didry, S., El Amrani, M., Autret-lambert, C. & Megriche, A. Brilliant effect of Ni substitution in the appearance of high dielectric constant in CaCu2.9Ni0.1Ti3.9Ni0.1O12 ceramics. *J. Alloys Compd.* **765**, 927–935 (2018).
26. Huang, Y., Qiao, Y., Li, Y., He, J. & Zeng, H. Zn-Doped Calcium Copper Titanate Synthesized via Rapid Laser Sintering of Sol-Gel Derived Precursors. *Nanomaterials* **10**, 1163 (2020).

27. Valim, D. *et al.* Raman scattering and x-ray diffraction studies of polycrystalline Ca Cu 3 Ti 4 O 12 under high-pressure. *Phys. Rev. B* **70**, 132103 (2004).

28. He, L., Neaton, J. B., Cohen, M. H., Vanderbilt, D. & Homes, C. C. First-principles study of the structure and lattice dielectric response of CaCu 3 Ti 4 O 12. *Phys. Rev. B* **65**, 214112 (2002).

29. Subramanian, M. A., Li, D., Duan, N., Reisner, B. A. & Sleight, A. W. High Dielectric Constant in ACu3Ti4O12 and ACu3Ti3FeO12 Phases. *J. Solid State Chem.* **151**, 323–325 (2000).

30. Ramirez, A. P. *et al.* Giant dielectric constant response in a copper-titanate. *Solid State Commun.* **115**, 217–220 (2000).

31. Karmakar, S., Varma, S. & Behera, D. Investigation of structural and electrical transport properties of nano-flower shaped NiCo2O4 supercapacitor electrode materials. *J. Alloys Compd.* **757**, 49–59 (2018).

32. Karmakar, S. & Behera, D. Non-overlapping small polaron tunneling conduction coupled dielectric relaxation in weak ferromagnetic $NiAl_2O_4$. *J. Phys. Condens. Matter* **31**, 245701 (2019).

33. Jebli, M. *et al.* Structural and morphological studies, and temperature/frequency dependence of electrical conductivity of $Ba_{0.97}La_{0.02}Ti_{1-x}Nb_{4x/5}O_3$ perovskite ceramics. *RSC Adv.* **11**, 23664–23678 (2021).

34. Kim, C. H. *et al.* Effect of Mn doping on the temperature-dependent anomalous giant dielectric behavior of CaCu 3 Ti 4 O 12. *Phys. Rev. B* **85**, 245210 (2012).

35. Liu, L. *et al.* Localized polarons and conductive charge carriers: Understanding CaCu 3 Ti 4 O 12 over a broad temperature range. *Phys. Rev. B* **99**, 094110 (2019).

36. Tang, R. *et al.* Dielectric relaxation, resonance and scaling behaviors in Sr3Co2Fe24O41 hexaferrite. *Sci. Rep.* **5**, 13645 (2015).

37. Karmakar, S. *et al.* Electric field emission and anomalies of electrical conductivity above room temperature in heterogeneous NiO-SnO2 nano-ceramic composites. *J. Appl. Phys.* **127**, 034102 (2020).

38. Raymond, O., Font, R., Suárez-Almodovar, N., Portelles, J. & Siqueiros, J. M. Frequency-temperature response of ferroelectromagnetic Pb(Fe1⁄2Nb1⁄2)O3 ceramics obtained by different precursors. Part II. Impedance spectroscopy characterization. *J. Appl. Phys.* **97**, 084108 (2005).

39. Schmidt, R. & Sinclair, D. C. CaCu3Ti4O12 (CCTO) ceramics for capacitor applications. Preprint at https://doi.org/10.48550/ARXIV.1402.1621 (2014).

40. Schmidt, R., Pandey, S., Fiorenza, P. & Sinclair, D. C. Non-stoichiometry in "CaCu3Ti4O12" (CCTO) ceramics. *RSC Adv.* **3**, 14580 (2013).

41. Karmakar, S. *et al.* A Study on Optical and Dielectric Properties of Ni-ZnO nanocomposite. *Mater. Sci. Semicond. Process.* **88**, 198–206 (2018).

42. Karmakar, S., Tyagi, H., Mohapatra, D. P. & Behera, D. Dielectric relaxation behavior and overlapping large polaron tunneling conduction mechanism in NiO–PbO μ-cauliflower composites. *J. Alloys Compd.* **851**, 156789 (2021).

43. Koval, V. *et al.* Dielectric relaxation and conductivity phenomena in ferroelectric ceramics at high temperatures. *J. Eur. Ceram. Soc.* **44**, 2886–2902 (2024).

44. Filipič, C., Levstik, A., Kutnjak, Z., Umek, P. & Arčon, D. Fluctuation-induced tunneling in TiO2-derived nanotube pellets. *J. Appl. Phys.* **101**, 084308 (2007).

45. Karmakar, S. *et al.* Superior field emission and alternating current conduction mechanisms for grains and grain boundaries in an NiO-[CdO]2 nanocomposite. *J. Phys. Chem. Solids* **142**, 109462 (2020).

46. Karmakar, S. *et al.* Temperature-driven complex dielectric and polaron-hopping mediated electrical conduction in aurivillius Gd2MoO6. *J. Alloys Compd.* **955**, 170271 (2023).

47. Tselev, A. *et al.* Evidence for power-law frequency dependence of intrinsic dielectric response in the Ca Cu 3 Ti 4 O 12. *Phys. Rev. B* **70**, 144101 (2004).

48. Lunkenheimer, P. *et al.* Origin of apparent colossal dielectric constants. *Phys. Rev. B* **66**, 052105 (2002).

49. Yong, J., Winie, T., Khandaker, M. U., Chen, Y. & Woo, H. J. Various types of A.C conduction mechanism models for solid polymer electrolytes (SPE): A review. *J. Power Sources* **645**, 237217 (2025).

50. Jebli, M. *et al.* Structural and morphological studies, and temperature/frequency dependence of electrical conductivity of $Ba_{0.97}$ $La_{0.02}$ Ti_{1-x} $Nb_{4x/5}$ O_3 perovskite ceramics. *RSC Adv.* **11**, 23664–23678 (2021).

51. Pradhan, A. K., Saha, S. & Nath, T. K. AC and DC electrical conductivity, dielectric and magnetic properties of Co0.65Zn0.35Fe2−x Mo x O4 (x = 0.0, 0.1 and 0.2) ferrites. *Appl. Phys. A* **123**, 715 (2017).

52. Karmakar, S. & Behera, D. Band-correlated barrier-hopping conduction in α-NiMoO4 micro-crystals and comparison of its energy storage performance with MWCNT-integrated complex. *J. Mater. Sci. Mater. Electron.* **31**, 5336–5352 (2020).

53. Funke, K. Jump relaxation in solid electrolytes. *Prog. Solid State Chem.* **22**, 111–195 (1993).

54. Gupta, P., Mahapatra, P. K. & Choudhary, R. N. P. $TbFeO_3$ Ceramic: An Exciting Colossal Dielectric with Ferroelectric Properties. *Phys. Status Solidi B* **257**, 1900236 (2020).

55. Hota, S. S., Panda, D. & Choudhary, R. N. P. Studies of structural, dielectric, electrical, and optical properties of a multi-doped novel complex perovskite (Bi1/2Na1/2)(Fe1/3Mn1/3W1/3)O3 ceramic for opto-electronic application. *Chin. J. Phys.* **87**, 430–451 (2024).

56. Karmakar, S. *et al.* Upheaval of Negative Dielectric Permittivity and Semiconductor to Metallic Transition in a Thermally Induced Sn-Doped β-Ga_2 O_3 (−201) Single Crystal. *ACS Appl. Mater. Interfaces* **16**, 48488–48501 (2024).

57. Zhang, J. L. *et al.* Dielectric dispersion of CaCu3Ti4O12 ceramics at high temperatures. *Appl. Phys. Lett.* **87**, 142901 (2005).

58. Cole, K. S. & Cole, R. H. Dispersion and Absorption in Dielectrics I. Alternating Current Characteristics. *J. Chem. Phys.* **9**, 341–351 (1941).

59. Holm, S. Time domain characterization of the Cole-Cole dielectric model. *J. Electr. Bioimpedance* **11**, 101–105 (2020).

60. Li, J. Y., Zhao, X. T., Li, S. T. & Alim, M. A. Intrinsic and extrinsic relaxation of CaCu3Ti4O12 ceramics: Effect of sintering. *J. Appl. Phys.* **108**, 104104 (2010).

61. Yadav, B., Kar, K. K., Ghorai, M. K., Kumar, D. & Yadav, D. Impact of defect migration on electrical and dielectric properties in molten salt synthesized CaCu3Ti4O12 and customizing the properties by compositional engineering with Mg doping. *Mater. Chem. Phys.* **281**, 125893 (2022).

62. Costa, S. I. R., Li, M., Frade, J. R. & Sinclair, D. C. Modulus spectroscopy of CaCu3Ti4O12 ceramics: clues to the internal barrier layer capacitance mechanism. *RSC Adv.* **3**, 7030 (2013).

63. Slimi, H., Oueslati, A. & Aydi, A. Vibrational studies, dielectric, and electrical conductivity in (Ba0.95Ca0.05)0.1(Ti0.8Sn0.2)0.1Na0.9Nb0.9O3 ferroelectric ceramic. *Appl. Phys. A* **125**, 510 (2019).

64. Hajlaoui, S., Chaabane, I., Oueslati, A. & Guidara, K. Electrical transport properties and modulus behavior of the organic–inorganic [N(C3H7)4]2SnCl6 compound. *Phys. B Condens. Matter* **474**, 90–96 (2015).

65. Singh, L., Rai, U. S. & Mandal, K. D. Dielectric, modulus and impedance spectroscopic studies of nanostructured CaCu2.70Mg0.30Ti4O12 electro-ceramic synthesized by modified sol–gel route. *J. Alloys Compd.* **555**, 176–183 (2013).

66. J.K., L. *et al.* Dielectric Properties of BaTi2O5 Glass. *J. Korean Phys. Soc.* **47**, 267 (2005).